The Astrophysical Journal Supplement Series, 269:60 (11pp), 2023 December https://doi.org/10.3847/1538-4365/ad04d5

Optical Monitoring and Intraday Variabilities of BL Lacertae

Y. H. Yuan[1,2], G. J. Du[1,2], J. H. Fan[1,2], Y. Liu[1,2], J. H. Yang[3], G. Z. Ding[1,2], and Z. Y. Pei[1,2,3]
[1] Center for Astrophysics, Guangzhou University, Guangzhou, Guangdong, 510006, People's Republic of China; yh_yuan@gzhu.edu.cn
[2] Astronomy Science and Technology Research Laboratory of Department of Education of Guangdong Province, Guangzhou 510006, People's Republic of China
[3] College of Mathematics and Physics Science, Hunan University of Arts and Science, Changde 415000, People's Republic of China
Received 2023 July 22; revised 2023 October 3; accepted 2023 October 14; published 2023 December 7

Abstract

BL Lacertae is a key monitoring target of the 1.26 m National Astronomical Observatory–Guangzhou University Infrared/Optical telescope. Within the monitored duration from 2020 September 4 to 2022 September 28, we report 13,948 observations at the *g*, *r*, and *i* bands (*g* band: 4498, *r* band: 4866, *i* band: 4584). (1) In the monitored duration, this source is located in a very bright and variable state. The maximum variabilities are $\Delta m_g = 2.013 \pm 0.073$ mag at *g* band, $\Delta m_r = 1.900 \pm 0.049$ mag at *r* band, and $\Delta m_i = 2.279 \pm 0.089$ mag at *i* band. (2) Among the *gri* intraday lightcurves, there are 104 portions of data sets displaying intraday variabilities (IDVs), with the IDV timescales (ΔT) being in the range of 15.84–375.84 minutes and the biggest variable value $\Delta m = 0.430 \pm 0.041$ mag. (3) The distributions of ΔT show frequency-dependent behavior, and with the frequency increasing, ΔT tend to be shorter. The variable rates ($V = \frac{\Delta m}{\Delta T}$) from the *g* band are more intense than the values (V_r) from the *r* band, but are more stable than the values (V_i) from the *i* band. (4) On three days (2020 September 7, 2020 September 19, and 2022 September 7), we find the intraday periodic oscillations, whose periods are around 150 minutes, 232 minutes, and 150 minutes, respectively, and which might come from the source "flickering." (5) Based on the distributions between flux densities (F_{gri}) and spectral indices (α), they show the bluer-when-brighter behaviors and some uneven locations, which should come from the ministructures of the jet, the shock-induced particle acceleration, or magnetic reconnection in the jet.

Unified Astronomy Thesaurus concepts: Galaxies (573); Blazars (164); CCD photometry (208)

Supporting material: machine-readable table

1. Introduction

Blazars are a subclass of active galactic nuclei (AGNs), and display some special properties, such as core dominance, high and variable polarization, superluminal motion, violently optical variability, and other extreme natures of radiation (Ulrich et al. 1997). On the basis of their optical emission line and the compact radio morphologies (e.g., Urry & Padovani 1995; Weaver et al. 2020), blazars can be divided into BL Lacertae (BL Lac) objects and flat-spectrum radio spectrum, and the former are characterized by a featureless optical or weak emission line (Stickel et al. 1991).

Optical variability is a typical property of blazars, with a timescale from minutes to years. The optical variabilities can be divided into three types, notably intraday optical variability (IDV or microvariability), with a timescale of around 1 day; short-term variability, with a timescale from days to months; and long-term variability, with a timescale of years (Fan 2005).

Generally, IDVs are nonperiodic and lack regularity, which might originate from the central black hole, the jets, the instability of the accretion disk or the interstellar medium, and so on. Recently, some studies supply us with the periodic and regular IDVs of blazars. S5 0716+714 displayed some IDV periods at the optical band: ∼25 minutes and ∼3 minutes (Gupta et al. 2009), 50 minutes (Hong et al. 2018), and ≈185.78 minutes (Liu et al. 2021). PKS 0735+178 showed an IDV periodic oscillation of 66.9 ± 4.1 minutes (Yuan & Fan 2021). OJ 287 displayed the following periodic results: ∼40 minutes at the radio band (Visvanathan & Elliot 1973), 15.7 minutes at the radio band (Valtaoja et al. 1985), and 35 minutes at the 7 mm band (Kinzel et al. 1988). 3C 273 gave some IDV periods: ∼55 minutes in the XMM-Newton lightcurve (Espaillat et al. 2008) and ∼60 minutes and ∼80 minutes at the optical band (Liu et al. 2021). PKS 2155-304 reported some quasiperiodic oscillations (QPOs): 0.7 days in the UV and optical bands (Urry et al. 1993), and ∼4.6 hr in the XMM-Newton X-ray lightcurve (Lachowicz et al. 2009). 3C 454.3 showed an IDV periodicity of 102 minutes from the optical lightcurve (Fan et al. 2019). The IDV timescales of 3C 454.3 displayed three denser regions: $\Delta T_1 = 17.18$ minutes, $\Delta T_2 = 34.91$ minutes, and $\Delta T_3 = 68.92$ minutes (Yuan et al. 2022).

BL Lacertae ($z = 0.069$, Miller et al. 1978) is the archetype of BL Lac objects, and is located in a huge elliptical galaxy and displays superluminal behaviors (Mutel & Phillips 1987; Vermeulen & Cohen 1994). Generally, it is classified as a low-frequency peaked blazar (Nilsson et al. 2018), but sometimes as an intermediate-frequency peaked blazar (Hervet et al. 2016).

BL Lacertae is a monitored target by many multiband comparisons covering from radio to the very high-energy γ-ray bands (Marscher et al. 2008; Raiteri et al. 2013; Weaver et al. 2020; Sahakyan & Giommi 2022, etc.). This source has been monitored for more than a century at the optical band, and shows extremely optical variabilities (e.g., Sitko et al. 1985). Fan et al. (1998) reported that the long-term variable values should be $\Delta m \approx 5$ mag at the *U*, *B*, and *V* bands, and $\Delta m \approx 2.5$ mag at the *R* and *I* bands. Meng et al. (2017) found the IDV

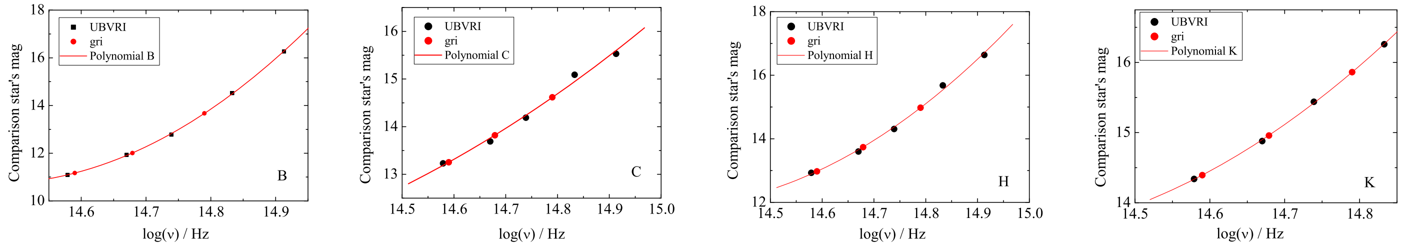

Figure 1. The g, r, and i fitting results of the four comparison stars. The black solid dots stand for U, B, V, R, and I data, the red solid dots stand for g, r, and i data, and the red lines stand for the least-square fitting curves.

Table 1
Comparison Stars of BL Lacertae (1ES 2200+420)

Comp (1)	U (error) (mag) (2)	B (error) (mag) (3)	V (error) (mag) (4)	R (error) (mag) (5)	I (error) (mag) (6)	g (mag) (7)	r (mag) (8)	i (mag) (9)
B	16.27 (0.09)	14.52 (0.04)	12.78 (0.04)	11.93 (0.05)	11.09 (0.06)	13.67	12.08	11.17
C	15.53 (0.06)	15.09 (0.03)	14.19 (0.03)	13.69 (0.03)	13.23 (0.04)	14.62	13.86	13.25
H	16.64 (0.08)	15.68 (0.03)	14.31 (0.05)	13.60 (0.03)	12.93 (0.04)	14.98	13.80	12.97
K	⋯	16.26 (0.05)	15.44 (0.03)	14.88 (0.05)	14.34 (0.10)	15.86	15.01	14.39

in the B, V, R, and I bands in 13 nights from 2012 to 2016. Weaver et al. (2020) reported a variability timescale ∼30 minutes at the optical bands observed by the Transiting Exoplanet Survey Satellite and 14.5 hr at the X-ray band.

BL Lacertae is one of the key detection targets of the 1.26 m National Astronomical Observatory–Guangzhou University Infrared/Optical telescope (NGT). Kalita et al. (2023) availed the observations monitored by NGT in the period of 2020 August to analyze the optical flux and spectral variabilities. Kalita et al. (2023) found the intraday variabilities (up to ∼30%), and a clear frequency-dependent pattern along symmetric timescales (∼11 days). These results can be explained in the context of shock-induced particle acceleration or the magnetic reconnection from the jet.

The long-term quasiperiodicities of BL Lacertae have been acclaimed by many works. Fan et al. (1998) reported that the quasiperiodicities should be 0.6, 0.88, 14, and 20 yr. A periodicity of ∼8 yr was found by Villata et al. (2004) and Villata et al. (2009). Sandrinelli et al. (2017) found a periodicity of about 680 days at the R band and γ-ray lightcurve. Papadakis et al. (2003) found that the variable timescales started to decline as the frequency decreased, and obtained a time delay ∼0.4 hr between the B band and the I band. The relations between the flux densities and spectra showed that the optical spectrum became flatter when the flux increased (Gaur et al. 2015). Itoh et al. (2016) found a positive correlation between optical and γ-ray flux variations.

In order to analyze the optical variabilities of BL Lacertae, we carry out monitoring and research. This paper is arranged as follows: in Section 2, we give the observations and data reductions; in Section 3, we analyze optical variability; in Section 4, we present discussions and conclusions.

2. Observations and Data Reductions

2.1. Photometry Process

We used the NGT, located at Xinglong station, National Astronomical Observatories, Chinese Academy of Sciences, to monitor the object (BL Lacertae). This telescope was equipped with three SBIG STT-8300M cameras with a CCD of 3326 × 2504 pixels and a field of view of 6.′0 × 4.′5. These filters adopt standard Sloan Digital Sky Survey (SDSS) g, r, and i bands. The detailed description of this telescope was given in Fan et al. (2019).

We used the following procedures to carry out the image reduction: (1) obtain the bias images at the beginning and the end of the observation night; (2) take the flat-field images at dusk and dawn; (3) obtain photometry after the bias and flat-field corrections.

We collected the standard stars from Smith et al. (1985), and noted them as "B," "C," "H," and "K." The comparison stars have been listed in Table 1, where column (1) gives the order number of the comparison stars, and columns (2)–(6) give the comparison stars at the U, B, V, R, and I bands, in units of magnitude.

Based on the least-square fitting method, $m_\nu = a\log^2\nu + b\log\nu + c$, where m_ν was the magnitude at the ν band ($\nu = U$, B, V, R, and I), we calculated the g, r, and i magnitudes of every comparison star. The fitting processes have been noted in Figure 1, where the black solid dots stand for the U, B, R, V, and I magnitudes, the red solid dots stand for the g, r, and i magnitudes, and the red lines stand for the least-square fitting curves. The fitting results are noted in Table 1, where columns (7)–(9) give the g, r, and i magnitudes, in units of magnitude.

2.2. Data Reductions and Observations

The observations were monitored through the g, r, and i filters and the exposure time was 300 s at three bands. Within the same frame, there were four comparison stars C_i, $i = 1$, 2, 3, 4.

The observations were reduced by the following procedure. First, for any two comparison stars (c_i and c_j), the magnitudes of them were m_i and m_j, and the magnitude difference between them was $\Delta m_{ij} = m_i - m_j$, with the standard deviation being σ_{ij}. Second, we compared the standard deviation σ from any two arbitrary standard stars, and found that when the comparison stars were "B" and "C," the standard deviation reached the minimum. Third, we chose the two comparison stars (S_B and S_C) to calculate two object magnitudes ($m_{o|B}$ and

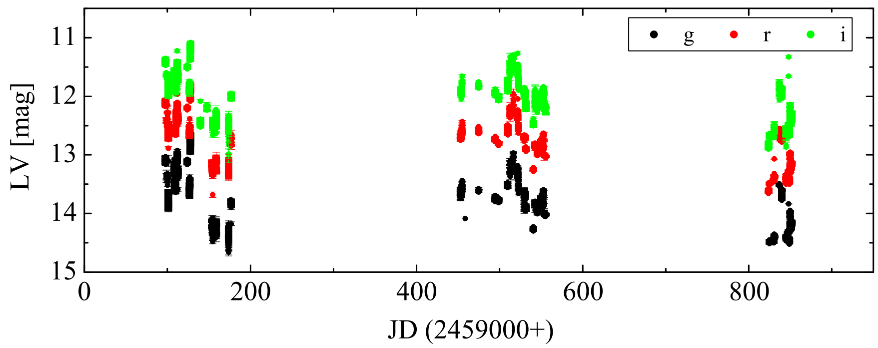

Figure 2. The g, r, and i lightcurves. The black solid dots stand for the g lightcurve, the red solid dots stand for the r lightcurve, and the green solid dots stand for the i lightcurve.

Table 2
The *gri* Observations of BL Lacertae (1ES 2200+420)

g-JD (+2459000) (1)	m_g (mag) (2)	σ_g (mag) (3)	r-JD (+2459000) (4)	m_r (mag) (5)	σ_r (mag) (6)	i-JD (+2459000) (7)	m_i (mag) (8)	σ_i (mag) (9)
97.691	13.104	0.029	97.691	12.106	0.027	97.691	11.403	0.027
97.692	13.111	0.029	97.692	12.085	0.027	97.692	11.383	0.027
97.693	13.118	0.029	97.693	12.108	0.027	97.693	11.406	0.027
97.695	13.111	0.029	97.695	12.117	0.027	97.695	11.414	0.027
97.696	13.117	0.029	97.696	12.114	0.027	97.696	11.412	0.027
97.697	13.125	0.029	97.697	12.110	0.027	97.697	11.408	0.027
97.698	13.124	0.029	97.698	12.122	0.027	97.698	11.419	0.027
97.699	13.131	0.029	97.699	12.123	0.027	97.699	11.421	0.027
97.701	13.140	0.029	97.701	12.127	0.027	97.701	11.424	0.027
97.702	13.121	0.029	97.702	12.111	0.027	97.702	11.409	0.027

(This table is available in its entirety in machine-readable form.)

$m_{o|C}$) based on the two comparison stars, and obtained the averaged value $m_o = \frac{1}{2}(m_{o|B} - m_{o|C})$ as the target magnitude at a time. The deviation of the magnitude difference $S_B - S_C$ from a certain night was taken as the corresponding uncertainty for the whole observation night.

The monitored activities contained 56 observational nights during the period from 2020 September 4 to 2022 September 28. The observations have been listed in Table 2, where column (1) is the Julian date (JD) of g-band observation; column (2) is the observed SDSS g-band AB magnitude, in units of magnitude; column (3) is σ_g, the uncertainty for m_g, in units of magnitude; column (4) is the JD of r-band observation; column (5) is the observed SDSS r-band AB magnitude, in units of magnitude; column (6) is σ_r, the uncertainty for m_r, in units of magnitude; column (7) is the JD of i-band observation; column (8) is the observed SDSS i-band AB magnitude, in units of magnitude; and column (9) is σ_i, the uncertainty for m_i, in units of magnitude.

At the g band there were 4497 observations, with coverage from 14.657 ± 0.067 to 12.644 ± 0.031 mag, and the largest variation $\Delta m_g = 2.013 \pm 0.074$ mag; at the r band, there were 4865 observations, with coverage from 13.680 ± 0.048 to 11.780 ± 0.013 mag, and the variation $\Delta m_r = 1.90 \pm 0.050$ mag; at the i band, there were 4578 observations, with coverage from 13.055 ± 0.082 to 10.776 ± 0.034 mag, and the variation $\Delta m_i = 1.971 \pm 0.087$ mag. We present the results in Figure 2, where the x-axis stands for JD (+2459000), the y-axis stands for lightcurve (LV), the black solid dots stand for the g lightcurve, the red solid dots stand for the r lightcurve, and the green solid dots stand for the i lightcurve.

3. Optical Variabilities

Many methods can be used to constrain the IDVs, such as the variability amplitude parameter (A_m), F-test, nested ANOVA, etc., which can be introduced as the following.

(1) *Variablity amplitude parameter* (A_m). Heidt & Wagner (1996) pointed out this method,

$$A_m = 100 \times \sqrt{(m_x - m_n)^2 - {\sigma_x}^2 - {\sigma_n}^2}\,(\%),$$

here $m_x \pm \sigma_x$ was the maximum value and $m_n \pm \sigma_n$ was the minimum value. When $A_m > 7.5\%$, the source displayed variable properties.

(2) *F-test*. de Diego (2010) introduced this method, which can be used to constrain the significance of a variation. This method can be described by $F = \frac{S_o^2}{S_t^2}$, where S_o^2 was the variance of the differential lightcurve values of the object and S_t^2 was the variance of the differential lightcurve values of the comparison stars.

(3) *Nested ANOVA*. The ANOVA test can compare the means of dispersion among the different groups of observations. The nested ANOVA test is an updated ANOVA test that can generate the different lightcurves of blazars based on several stars as the reference stars. The detailed introduction about this method is shown in de Diego et al. (2015).

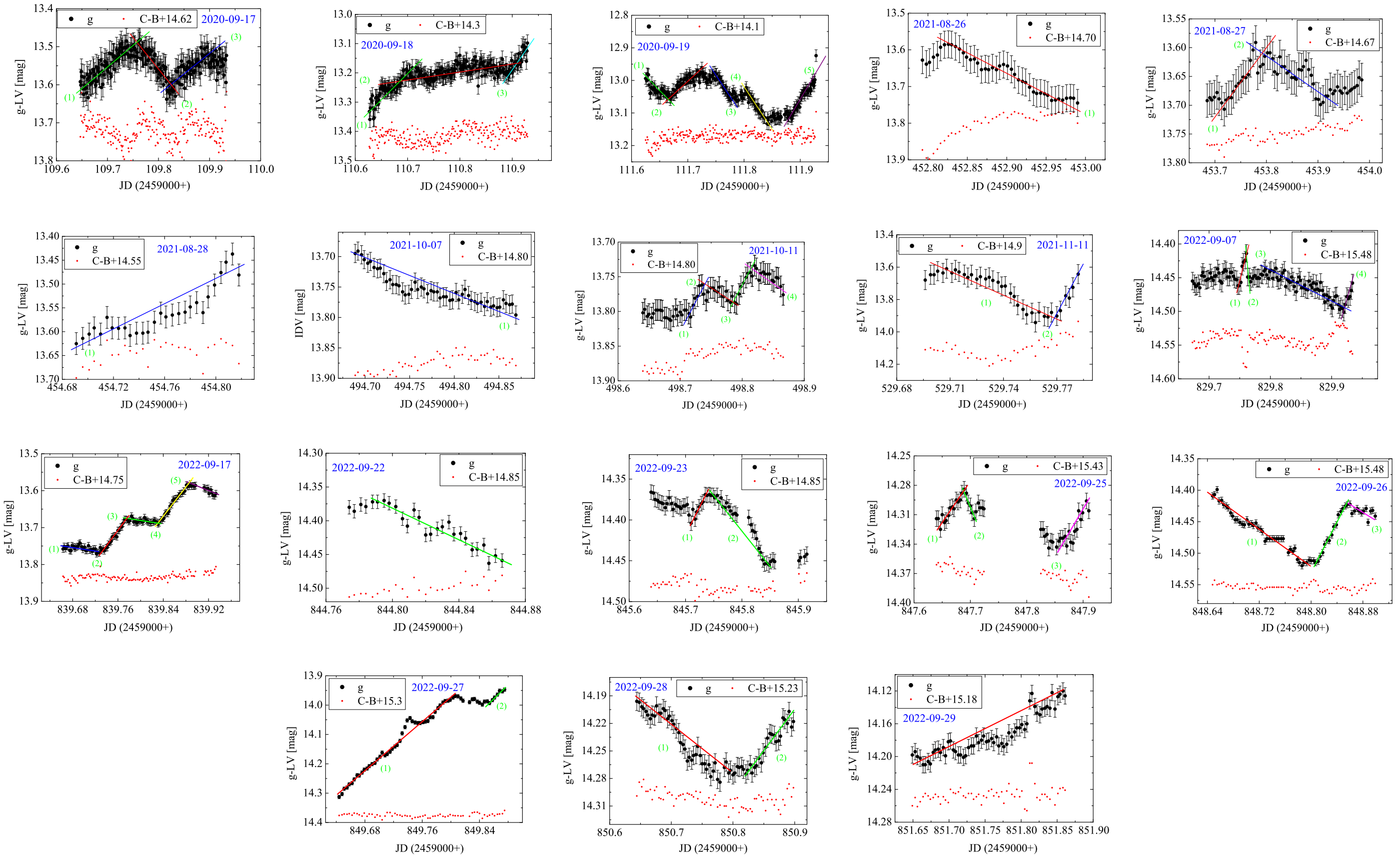

Figure 3. The IDVs at the g band. The black dots stand for the lightcurves, the red dots stand for the magnitude difference between two comparison stars, and the colored lines stand for the different stages.

For each intraday lightcurve, the number of freedom degrees (ν_O and ν_C) are the same and equal to $N-1$, where N is the pair number of observations. In order to check the variable values of a target, we can compare the F value from the observations with the critical value, $F_{C(\nu_O,\nu_C)}$. The F-test can be determined within two significance levels (1% and 0.1%). This method is consistent with the 2.6σ and 3σ detections, respectively (de Diego et al. 2015, Fan et al. 2017; Xiong et al. 2017).

On one single day, if there lies an IDV, we use the following procedure to obtain the variable values ($\Delta m \pm \sigma$) and variable timescales (ΔT). The intraday lightcurves are divided into some specific stages (brightening stages or dimming stages), which have been noted in Figures 3–5, and noted by "(1)," "(2)," "(3)," ⋯, where the x-axis stands for JD (+2459000), the y-axis stands for the lightcurve at the g band (g-LV), the lightcurve at the r band (r-LV), and the lightcurve at the i band (i-LV). On every stage, we calculate the most violent variability ($\Delta m \pm \sigma$), if $\Delta m > 2\sigma$ then $\Delta m \pm \sigma$ is the variable value, and the corresponding time span is variable timescales (ΔT). We use a linear regression to fit the relations between the timescale and magnitude variation, seeing the colored lines in Figures 3–5. The analyzed results are listed in Tables 3–5, where column (13) is the time rate of change, $V = \frac{\Delta m}{\Delta T}$, and column (14) is the ratio between Δm and σ, $\frac{\Delta m}{\sigma}$.

At the g band, among the 19 days there lie 41 stages displaying IDVs, with the biggest variation $\Delta m_g = 0.366 \pm 0.009$ mag. At the r band, among the 19 days there lie 43 stages displaying IDVs, with the biggest variation $\Delta m_r = 0.357 \pm 0.010$ mag. At the i band, among the 10 days there lie 20 stages displaying IDVs with the biggest variation $\Delta m_i = 0.222 \pm 0.041$ mag.

4. Discussion and Conclusion

4.1. Intraday Variabilities

Some studies (e.g., Meng et al. 2017; Weaver et al. 2020; Jorstad et al. 2022) reported the IDV properties of BL Lacertae. In this work, we obtain 104 stages displaying IDV properties at the gri bands, and calculate the variable timescale (ΔT) and variable value (Δm). Figure 6 displays the ΔT distributions (the left panel) and the Δm distributions (the right panel). With the help of a Gaussian function, we obtain the median values of ΔT and Δm at different bands. The median values of ΔT are $\overline{\Delta T_g} = 51.72 \pm 6.02$ minutes at the g band, $\overline{\Delta T_r} = 63.95 \pm 2.61$ minutes at the r band, and $\overline{\Delta T_i} = 75.50 \pm 3.87$ minutes at the i band. With the frequency increasing, ΔT becomes shorter. The median values of Δm are $\overline{\Delta m_g} = 0.09 \pm 0.005$ mag, $\overline{\Delta m_r} = 0.08 \pm 0.005$ mag, and $\overline{\Delta m_i} = 0.13 \pm 0.004$ mag. The variable values at the g band are consistent with the values from the r band, but are lower than the values at the i band.

We use the relation $V = \Delta m/\Delta T$ to calculate the time rates of the IDVs, and place the V distributions in Figure 7, seeing the black line (g band), red line (r band), and green line (i band). With the help of Gaussian fitting, we obtain the averaged values: at the g band $\overline{V_g} = 0.070 \pm 0.011$, with the correlation coefficient $r_g = 0.78$, at the r band

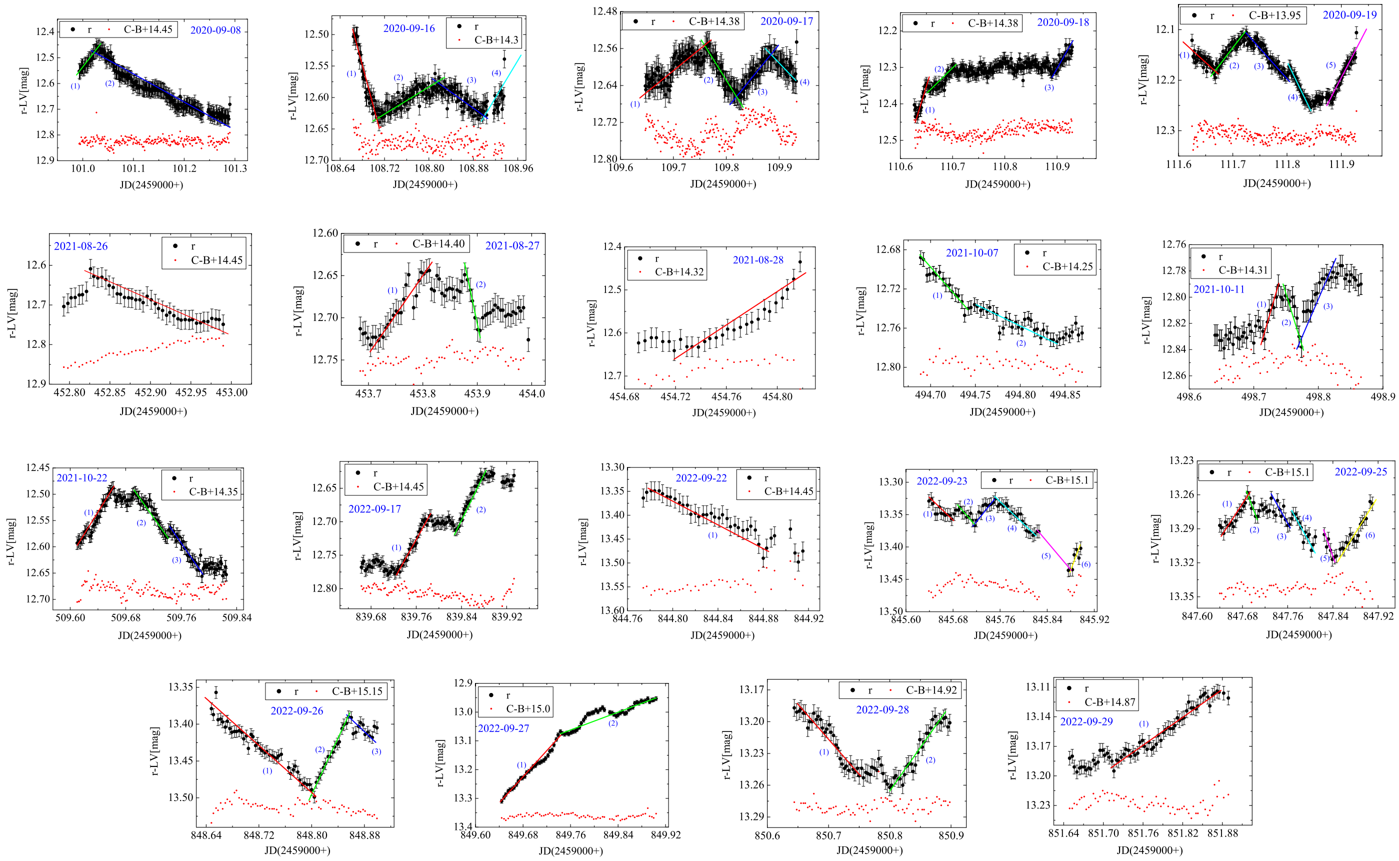

Figure 4. The IDVs at the r band. The black dots stand for the lightcurves, the red dots stand for the magnitude difference between two comparison stars, and the colored lines stand for the different stages.

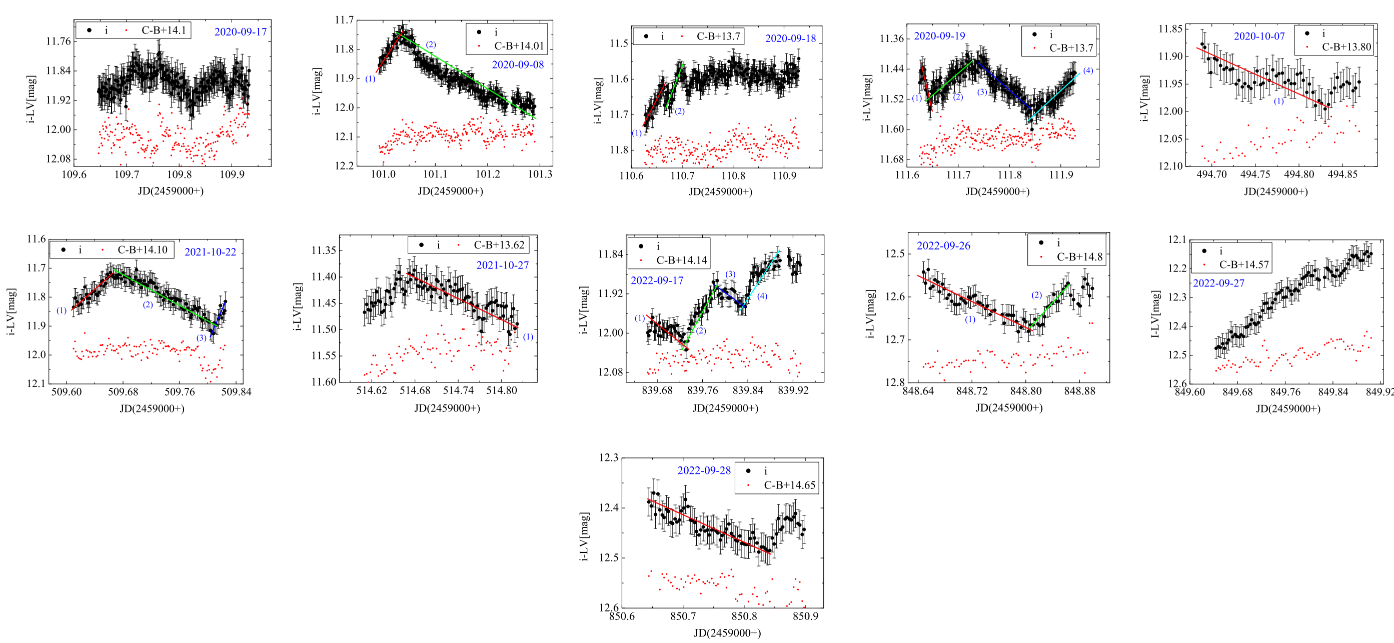

Figure 5. The IDVs at the i band. The black dots stand for the lightcurves, the red dots stand for the magnitude difference between two comparison stars, and the colored lines stand for the different stages.

$\overline{V_r} = 0.059 \pm 0.005$, with $r_r = 0.72$, and at the i band $\overline{V_i} = 0.076 \pm 0.005$, with $r_i = 0.78$. The variable rates from the g band are more intense than the values from the r band, but are more stable than the values from the i band.

Some sources displayed the intraday periodic oscillation. For example, Valtaoja et al. (1985) reported that OJ 287 had a possible period of 15.7 minutes at the radio band; Kinzel et al. (1988) used the 7 mm lightcurve to obtain a period of

Table 3
The IDV Results of BL Lacertae at the g Band

Date	N	A_m	F_1	F_2	$\overline{F}$	Nested ANOVA	$F^c_{(99)}$	$F^c_{(99.9)}$	Label	ΔT (hr)	$\Delta m \pm \sigma$ (mag)	V (mag hr^{-1})	$\frac{\Delta m}{\sigma}$
(1)	(2)	(3)	(4)	(5)	(6)	(7)	(8)	(9)	(10)	(11)	(12)	(13)	(14)
2020-9-17	237	14.99	1.05	0.96	1.00	5.509	1.36	1.5			0.157 ± 0.047		3.36
									(1)	2.45	0.153 ± 0.046	0.06	3.33
									(2)	1.25	0.157 ± 0.046	0.13	3.41
									(3)	1.90	0.137 ± 0.046	0.07	2.98
2020-9-18	250	25.80	3.56	2.09	2.83	19.22	1.34	1.48			0.261 ± 0.040		6.59
									(1)	1.94	0.177 ± 0.039	0.09	4.54
									(2)	3.67	0.131 ± 0.039	0.04	3.36
									(3)	0.89	0.113 ± 0.039	0.13	2.90
2020-9-19	240	20.85	1.03	0.98	1.01	13.9	1.35	1.49			0.210 ± 0.026		8.24
									(1)	0.98	0.079 ± 0.025	0.08	3.16
									(2)	1.34	0.097 ± 0.025	0.07	3.88
									(4)	0.84	0.095 ± 0.025	0.11	3.80
									(5)	1.03	0.194 ± 0.025	0.19	7.76
2021-8-26	43	15.12	2.70	1.64	2.17	105.3	2.08	2.66			0.160 ± 0.052		3.06
									(1)	3.94	0.160 ± 0.052	0.04	3.08
2021-8-27	66	10.85	0.92	1.09	1.01	1.504	1.79	2.17			0.116 ± 0.041		2.83
									(1)	1.46	0.116 ± 0.041	0.08	2.83
									(2)	3.02	0.108 ± 0.041	0.04	2.63
2021-8-28	28	18.52	0.99	0.98	0.98	2.774	2.51	3.44			0.188 ± 0.033		5.78
									(1)	2.93	0.188 ± 0.033	0.06	5.70
2021-10-6	52	10.28	3.02	1.96	2.49	9.652	1.94	2.41			0.105 ± 0.021		4.95
									(1)	4.25	0.105 ± 0.021	0.02	5.00
2021-10-11	130	7.61	0.86	0.64	0.75	70.06	1.51	1.73			0.079 ± 0.021		3.73
									(3)	0.70	0.055 ± 0.021	0.08	2.62
2021-11-11	37	32.13	5.26	2.34	3.80	4.86	2.21	2.89			0.332 ± 0.083		3.98
									(1)	1.20	0.332 ± 0.083	0.28	4.00
									(2)	0.29	0.259 ± 0.083	0.90	3.12
2022-9-7	111	8.50	1.92	1.67	1.80	4.18	1.56	1.81			0.087 ± 0.018		4.73
									(1)	0.29	0.048 ± 0.018	0.17	2.67
									(3)	2.66	0.065 ± 0.018	0.02	3.61
2022-9-17	110	18.86	2.74	2.47	2.60	19.13	1.57	1.82			0.189 ± 0.013		14.88
									(2)	1.49	0.102 ± 0.012	0.07	8.50
									(3)	0.53	0.039 ± 0.012	0.07	3.25
									(4)	1.37	0.108 ± 0.012	0.08	9.00
									(5)	1.03	0.032 ± 0.012	0.03	2.67
2022-9-22	27	9.19	1.79	2.71	2.25	8.77	2.55	3.53			0.093 ± 0.014		6.60
									(1)	1.51	0.093 ± 0.014	0.06	6.64
2022-9-23	62	8.81	1.96	1.71	1.84	5.443	1.83	2.24			0.089 ± 0.013		7.01
									(1)	0.60	0.035 ± 0.013	0.06	2.69
									(2)	0.74	0.086 ± 0.013	0.12	6.62
2022-9-24	53	13.61	1.22	1.16	1.19	22.7	1.92	2.40			0.137 ± 0.016		8.78
									(1)	0.50	0.067 ± 0.016	0.13	4.19
									(2)	0.26	0.053 ± 0.016	0.20	3.31
									(3)	0.34	0.053 ± 0.016	0.16	3.31
									(4)	1.37	0.112 ± 0.016	0.08	7.00
2022-9-25	75	96.49	0.52	0.50	0.51	7.93	1.73	2.07			0.060 ± 0.011		5.31
									(1)	1.01	0.041 ± 0.015	0.04	2.73
									(2)	0.43	0.030 ± 0.011	0.07	2.73
									(3)	1.27	0.047 ± 0.011	0.04	4.27
2022-9-26	71	12.08	1.28	1.24	1.26	6.773	1.75	2.12			0.121 ± 0.007		17.04
									(1)	3.14	0.121 ± 0.007	0.04	17.29
									(2)	1.27	0.093 ± 0.007	0.07	13.29
									(3)	0.67	0.029 ± 0.007	0.04	4.14
2022-9-27	65	36.59	2.01	1.93	1.97	1.774	1.80	2.19			0.366 ± 0.009		43.06
									(1)	1.61	0.344 ± 0.008	0.21	43.00
									(2)	0.50	0.026 ± 0.008	0.05	3.25
2022-9-28	73	8.69	0.91	0.86	0.88	14.76	1.74	2.09			0.088 ± 0.014		6.24
									(1)	0.86	0.088 ± 0.014	0.10	6.29
									(2)	0.58	0.068 ± 0.014	0.12	4.86
2022-9-29	61	8.89	0.75	0.72	0.73	1.578	1.84	2.25			0.090 ± 0.014		6.38
									(1)	0.53	0.090 ± 0.014	0.17	6.43

Table 4
The IDV Results of BL Lacertae at the r Band

Date	N	A_m	F_1	F_2	$\overline{F}$	Nested ANOVA	$F^c_{(99)}$	$F^c_{(99.9)}$	Label	ΔT (hr)	$\Delta m \pm \sigma$ (mag)	V (mag hr^{-1})	$\frac{\Delta m}{\sigma}$
(1)	(2)	(3)	(4)	(5)	(6)	(7)	(8)	(9)	(10)	(11)	(12)	(13)	(14)
2020-9-8	236	42.80	2.45	1.82	2.13	1.26	1.36	1.5			0.430 ± 0.041		10.48
									(2)	6.26	0.283 ± 0.041	0.05	6.90
2020-9-16	216	13.86	1.58	1.25	1.42	2.18	1.37	1.53			0.140 ± 0.020		7.07
									(1)	1.08	0.140 ± 0.019	0.13	7.37
						-			(2)	0.34	0.077 ± 0.019	0.23	4.05
									(3)	1.87	0.072 ± 0.019	0.04	3.79
2020-9-17	237	11.38	1.00	0.91	0.96	37.44	1.35	1.5			0.120 ± 0.038		3.14
									(2)	1.46	0.116 ± 0.038	0.08	3.05
2020-9-18	250	19.65	4.16	3.40	3.78	32.59	1.34	1.48			0.198 ± 0.024		8.24
									(1)	0.41	0.092 ± 0.024	0.23	3.83
									(2)	1.42	0.101 ± 0.024	0.07	4.21
									(3)	0.65	0.081 ± 0.024	0.13	3.38
2020-9-19	245	28.55	1.08	1.00	1.04	8.87	1.35	1.49			0.286 ± 0.017		16.85
									(1)	1.03	0.074 ± 0.017	0.07	4.35
									(2)	1.37	0.090 ± 0.017	0.07	5.29
									(3)	1.75	0.089 ± 0.017	0.05	5.24
									(4)	0.96	0.082 ± 0.017	0.09	4.82
									(5)	1.08	0.139 ± 0.017	0.13	8.18
2021-8-26	43	13.58	2.62	1.86	2.24	103.90	2.08	2.66			0.140 ± 0.034		4.12
									(1)	3.94	0.140 ± 0.034	0.04	4.12
2021-8-27	65	8.57	1.00	1.02	1.01	3.07	1.80	2.19			0.088 ± 0.020		4.44
									(1)	2.59	0.088 ± 0.020	0.03	4.40
									(2)	0.67	0.066 ± 0.020	0.10	3.30
2021-8-28	28	20.34	0.97	0.98	0.98	9.36	2.51	3.44			0.206 ± 0.033		6.33
									(1)	2.38	0.206 ± 0.033	0.09	6.24
2021-10-7	104	8.54	2.98	3.71	3.34	40.96	1.59	1.85			0.086 ± 0.010		8.69
									(1)	1.18	0.059 ± 0.009	0.05	6.56
									(2)	2.21	0.038 ± 0.009	0.02	4.22
2021-10-11	130	6.20	1.12	1.42	1.27	36.20	1.51	1.73			0.063 ± 0.011		5.57
									(1)	0.50	0.041 ± 0.011	0.08	3.73
									(2)	0.86	0.047 ± 0.011	0.05	4.27
									(3)	1.44	0.062 ± 0.011	0.04	5.64
2021-10-22	244	16.71	3.87	3.68	3.77	14.72	1.35	1.49			0.168 ± 0.017		9.90
									(1)	1.25	0.105 ± 0.017	0.08	6.18
									(2)	1.10	0.085 ± 0.017	0.08	5.00
									(3)	1.08	0.092 ± 0.017	0.09	5.41
2022-9-17	110	15.25	3.05	2.47	2.76	10.91	1.57	1.82			0.153 ± 0.013		12.02
									(1)	1.49	0.086 ± 0.013	0.06	6.62
									(2)	1.03	0.083 ± 0.013	0.08	6.38
2022-9-22	38	14.66	1.17	1.11	1.14	6.44	2.18	2.84			0.149 ± 0.027		5.55
									(1)	2.38	0.141 ± 0.027	0.06	5.22
2022-9-23	61	10.91	7.70	7.69	7.70	14.03	1.84	2.25			0.110 ± 0.014		7.78
									(3)	0.84	0.042 ± 0.014	0.05	3.00
									(4)	1.54	0.056 ± 0.014	0.04	4.00
									(5)	1.27	0.060 ± 0.014	0.05	4.29
2022-9-25	72	5.84	1.29	1.30	1.29	8.53	1.75	2.11			0.059 ± 0.008		6.95
									(1)	1.01	0.036 ± 0.008	0.04	4.50
									(3)	0.70	0.024 ± 0.008	0.03	3.00
									(4)	0.77	0.032 ± 0.008	0.04	4.00
2022-9-26	70	14.15	0.67	0.67	0.67	1.27	1.76	2.13			0.142 ± 0.011		12.55
									(1)	3.58	0.142 ± 0.011	0.04	12.91
									(2)	1.18	0.089 ± 0.011	0.08	8.09
2022-9-27	73	35.69	2.21	2.18	2.20	9.69	1.74	2.09			0.357 ± 0.010		36.06
									(1)	2.38	0.242 ± 0.010	0.10	24.20
									(2)	3.70	0.142 ± 0.010	0.04	14.20
2022-9-28	73	7.41	1.53	1.41	1.47	8.15	1.73	2.09			0.075 ± 0.011		6.63
									(1)	2.71	0.066 ± 0.011	0.02	6.00
									(2)	1.78	0.067 ± 0.011	0.04	6.09
2022-9-29	67	8.14	0.66	0.68	0.67	6.38	1.78	2.16			0.082 ± 0.010		8.28
									(1)	3.74	0.081 ± 0.010	0.02	8.10

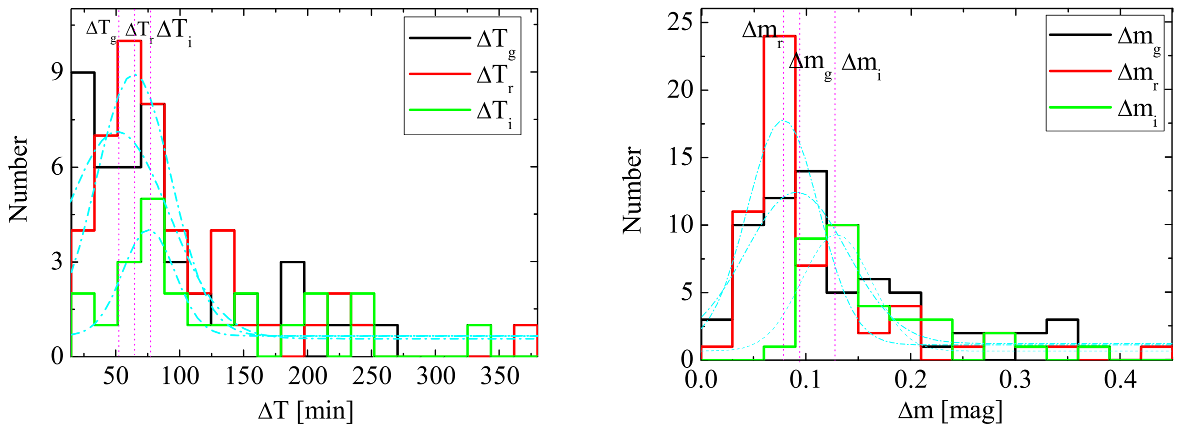

Figure 6. The ΔT and Δm distributions at the *gri* bands. The black, red, and green lines stand for the values from the *g* band, *r* band, and *i* band, respectively. The cyan lines stand for the Gaussian fitting.

Table 5
The IDV Results of BL Lacertae at the *i* Band

Date	N	A_m	F_1	F_2	$\overline{F}$	Nested ANOVA	$F^c_{(99)}$	$F^c_{(99.9)}$	Label	ΔT (hr)	$\Delta m \pm \sigma$ (mag)	V (mag hr^{-1})	$\frac{\Delta m}{\sigma}$
(1)	(2)	(3)	(4)	(5)	(6)	(7)	(8)	(9)	(10)	(11)	(12)	(13)	(14)
2020-9-8	235	28.65	1.99	1.93	1.96	12.68	1.36	1.5			0.289 ± 0.038		7.57
									(1)	1.03	0.133 ± 0.038	0.13	3.50
									(2)	5.50	0.289 ± 0.038	0.05	7.61
2020-9-17	250	18.51	4.09	1.94	3.01	17.01	1.34	1.48			0.189 ± 0.038		4.95
									(1)	0.84	0.126 ± 0.038	0.15	3.32
									(2)	0.94	0.107 ± 0.038	0.11	2.82
2020-9-18	246	19.50	1.08	1.07	1.08	27.64	1.35	1.49			0.376 ± 0.04		9.50
									(1)	0.36	0.112 ± 0.039	0.31	2.87
									(2)	1.73	0.146 ± 0.039	0.08	3.74
									(3)	2.40	0.194 ± 0.039	0.08	4.97
									(4)	1.97	0.152 ± 0.039	0.08	3.90
2020-10-4	201	30.02	2.06	2.13	2.10	2.13	1.39	1.55			0.303 ± 0.041		7.39
									(1)	0.94	0.222 ± 0.041	0.24	5.41
									(2)	1.22	0.126 ± 0.041	0.10	3.07
									(3)	2.38	0.16 ± 0.041	0.07	3.90
2021-10-6	52	11.17	6.37	1.36	3.87	25.19	1.94	2.42			0.118 ± 0.038		3.09
									(1)	3.38	0.118 ± 0.038	0.03	3.11
2021-10-21	122	21.60	2.80	3.82	3.31	11.42	1.34	1.49			0.221 ± 0.047		4.74
									(1)	1.25	0.12 ± 0.047	0.10	2.55
									(2)	2.62	0.221 ± 0.047	0.08	4.70
									(3)	0.41	0.111 ± 0.047	0.27	2.36
2021-10-26	90	11.63	4.99	1.76	3.38	13.29	1.42	1.59			0.122 ± 0.037		3.32
									(1)	3.19	0.122 ± 0.036	0.04	3.39
2021-11-10	50	16.20	1.87	2.62	2.25	14.26	1.96	2.46			0.169 ± 0.048		3.51
									(1)	1.58	0.166 ± 0.048	0.10	3.46
2022-9-16	110	19.03	2.71	3.31	3.01	2.39	1.57	1.82			0.192 ± 0.025		7.54
									(1)	1.42	0.066 ± 0.025	0.05	2.64
									(2)	1.32	0.141 ± 0.025	0.11	5.64
									(4)	1.37	0.104 ± 0.025	0.08	4.16
2022-9-25	69	14.10	1.20	1.33	1.26	12.28	1.77	2.14			0.145 ± 0.034		4.27
									(1)	3.91	0.145 ± 0.034	0.04	4.26
									(2)	3.58	0.144 ± 0.034	0.04	4.24
2022-9-27	73	11.12	0.94	1.11	1.02	4.59	2.09	1.74			0.118 ± 0.04		2.98
									(1)	4.13	0.118 ± 0.039	0.03	3.03

35 minutes. In PKS 0735 + 178, Yuan & Fan (2021) reported a period of 66.9 ± 4.1 minutes based on the optical lightcurve on 2016 January 6. In BL Lacertae, Jorstad et al. (2022) reported a QPO of about 13 hr during the 56 highest states of the outburst calculated by the optical flux, optical linear polarization, and γ-ray flux.

We checked the intraday lightcurves and used the REDFIT program to study the periodic properties. The REDFIT

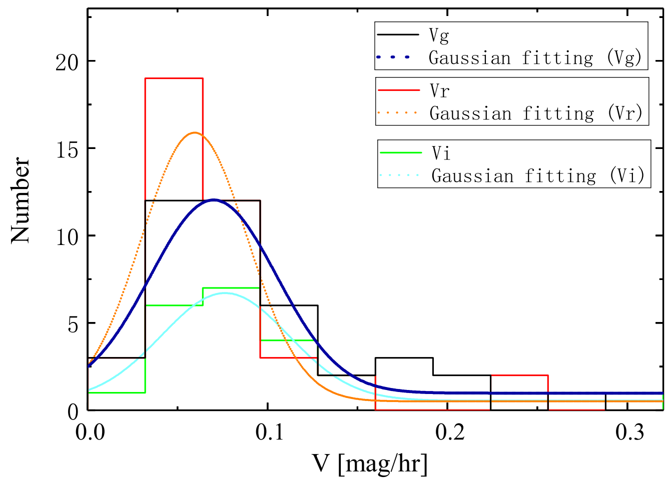

Figure 7. The distributions of the time rates of the IDVs at the *gri* bands. The black, red, and green lines stand for the values from the *g* band, *r* band and *i* band, respectively.

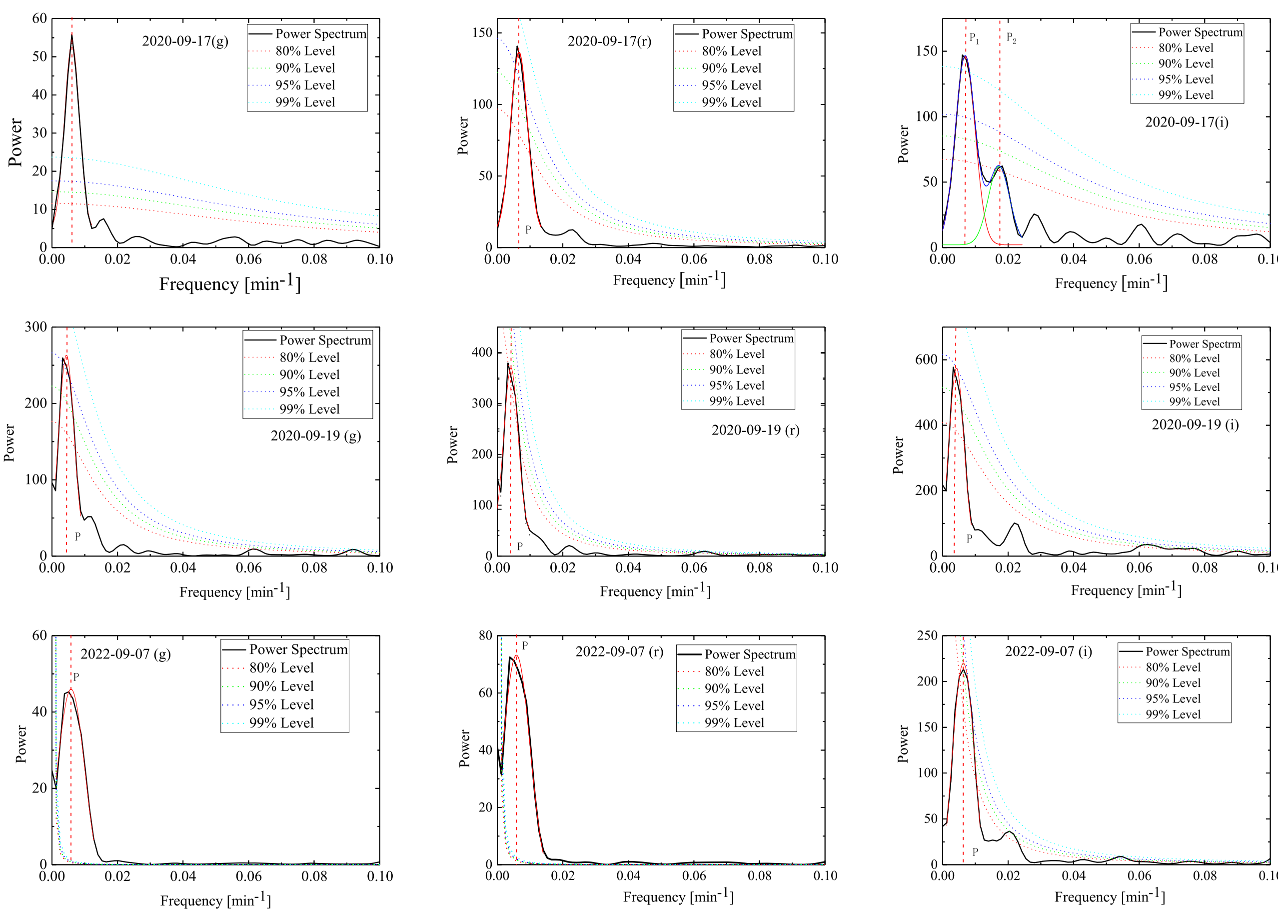

Figure 8. The intraday periodic results calculated by the the REDFIT program, where the black lines stand for the signal, the colored lines stand for the Gaussian fitting, and the colored dotted lines stand for the theoretical red-noise spectra of 80%, 90%, 95%, and 99% significance levels, respectively.

program used in this work is cited from Schulz & Mudelsee (2002), which is based on the Lomb–Scargle periodogram (Lomb 1976; Scargle 1982). The REDFIT program can directly estimate the first-order autoregressive (AR1) parameter from unevenly spaced time series, and the estimated AR1 model can be transformed from the time domain to the frequency domain. This program provides a confidence level for systematic deviation between the theoretical red-noise spectrum and the power spectrum (Lomb–Scargle Fourier transform).

The error can be obtained by the FWHM. The red-noise spectrum used to judge the REDFIT results is based on AR1. Based on the REDFIT method, the analyzed results have been shown in Figure 8, where the black lines stand for the power

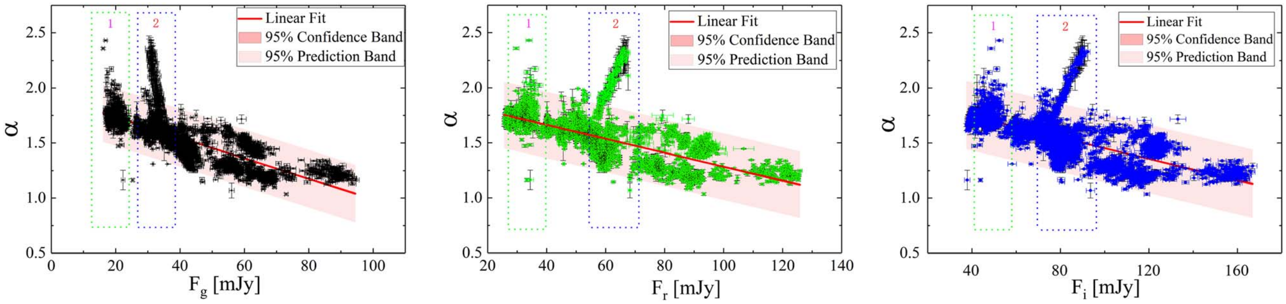

Figure 9. The correlation relations between the flux densities (F_{gri}) and spectral indices (α), where the light red area stands for the 95% confidence band, and the dark red area stands for the 95% prediction band.

spectrum signal and the colored dotted lines stand for the 80%, 90%, 95%, and 99% red-noise levels, respectively. We use the Gaussian function to fit the signal peak and obtain the periods.

Finally, on three days (2020 September 7, 2020 September 19, and 2022 September 7), we found the intraday periodic oscillations. On 2020 September 7, the periods are $P_g = 163.40 \pm 47.66$ minutes at the g band, $P_r = 150.60 \pm 50.60$ minutes at the r band, and $_{Pi} = 144.51 \pm 37.67$ minutes, 58.82 ± 7.01 minutes at the i band; seeing the upper three panels in Figure 8. On this day, the periods from different bands are consistent with each other, which are around 150 minutes. On 2020 September 19, the periods at the three bands are $P_g = 226.76 \pm 72.91$ minutes, $P_r = 232.56 \pm 78.71$ minutes, and $_{Pi} = 235.29 \pm 80.73$ minutes, which are consistent with each other, with a median of 232 minutes. On 2022 September 7, the periods at the three bands are $P_g = 171.82 \pm 64.29$ minutes, $P_r = 170.94 \pm 62.24$ minutes, and $_{Pi} = 131.75 \pm 27.59$ minutes, which are consistent with each other, with a median of 150 minutes, and similar to the period on 2020 September 7.

Within the range of error, the periods from different bands are consistent, $P \approx 131$–235 minutes, which is different from the exposure time (300 s) in each filter. So the intraday periodic oscillations should not come from the observation mode, but from the source "flickering." During our monitored duration, we obtain two types of IDVs: no periodic IDVs and periodic oscillations, but the physical origin of two types of IDVs are not clear and definite.

4.2. The Relations between Flux Densities and Spectral Indices

We use the following processes to analyze the relations between the spectral indices (α) and flux densities (F_{gri}).

1. First, based on NED[4], we make the Galactic extinction correlation, A_g = 1.086 mag, A_g = 0.751 mag, and A_g = 0.558 mag.
2. Second, we convert the magnitude (m_ν) into flux density (F_ν), here ν is the frequency ($\nu = 6.17 \times 10^{14}$ Hz for g, $\nu = 4.77 \times 10^{14}$ Hz for r, and $\nu = 3.89 \times 10^{14}$ Hz for i).
3. Third, we use the relation $F_\nu \propto \nu^{-\alpha}$ to calculate the spectral indices (α), here F_g, F_r, and F_i are the gri flux densities at the same time.
4. Lastly, we use the linear correlation to analyze the relations between α and F_ν, $F_\nu = (k \pm \Delta k)\alpha + (b \pm \Delta b)$, with the correlation coefficient (r) and the chance probability (p). We use the confidence band and the prediction band to estimate the fitting interval, which is a range of intervals used to estimate a population parameter, and can usually be expressed as a lower bound and an upper bound. The so-called confidence band is the interval formed by the upper and lower bounds of the confidence upper and lower bounds of the statistics, respectively. The prediction band is an interval under the condition of a given significance level χ, with the probability of F_ν corresponding to a specific α lying in this interval being $1 - \chi$.

Based on our observations, the correlations between the flux densities (F_{gri}) and spectral indices (α) are $\alpha =(-9.35 \pm 0.12) \times 10^{-3} F_g + (1.92 \pm 0.01)$, with the correlation coefficient $r = -0.77$, the chance probability $p < 0.001$ at the g band; $\alpha = (-6.34 \pm 0.11) \times 10^{-3} F_r + (1.92 \pm 0.01)$, with $r = -0.68$, $p < 0.001$ at the r band; $\alpha = (-4.85 \pm 0.08) \times 10^{-3} F_i + (1.94 \pm 0.01)$, with $r = -0.66$, $p < 0.001$ at the i band. These results display anticorrelations between F_{gri} and α at the whole bands (gri), which have been plotted in Figure 9, where the red lines stand for the linear fitting, the light red regions stand for the 95% confidence band, and the dark red area stands for the 95% prediction band. Our results display typical bluer-when-brighter (BWB) behavior: when the brightness is greater, the spectra become bluer.

Among the distributions between α and F_{gri}, we can find some separate structures; see the rectangular area in Figure 9. These structures display obvious discrepancies at different bands, which can be explained as the models of two components. The first one comes from the thermal component, which displays a weak and relative stable variability. The second one originates from the synchrotron emission component, which displays strong and highly variable properties. In the low state, thermal emission dominates the total radiation, while in the high state, the synchrotron emission dominates the total radiation.

Kalita et al. (2023) found the time evolution of color in this source. We check the intraday distributions between the magnitude and color index, and find that there lie two days (2020 September 18 and 2022 September 27) displaying the time evolution of color (see Figure 10) where the rectangular boxes mark the time ranges of the observations (JD +2459000). On 2020 September 18, in the two evolution stages, the fitting slope is about 0.59, but the evolution time is different. On 2022 September 27, in the two evolution stages, the fitting slope is about 0.40, and the evolution time is about 2 hr. The main reason for the phenomenon of time evolution of color might be that there is shock-induced particle acceleration or magnetic reconnection in the jet.

[4] http://ned.ipac.caltech.edu

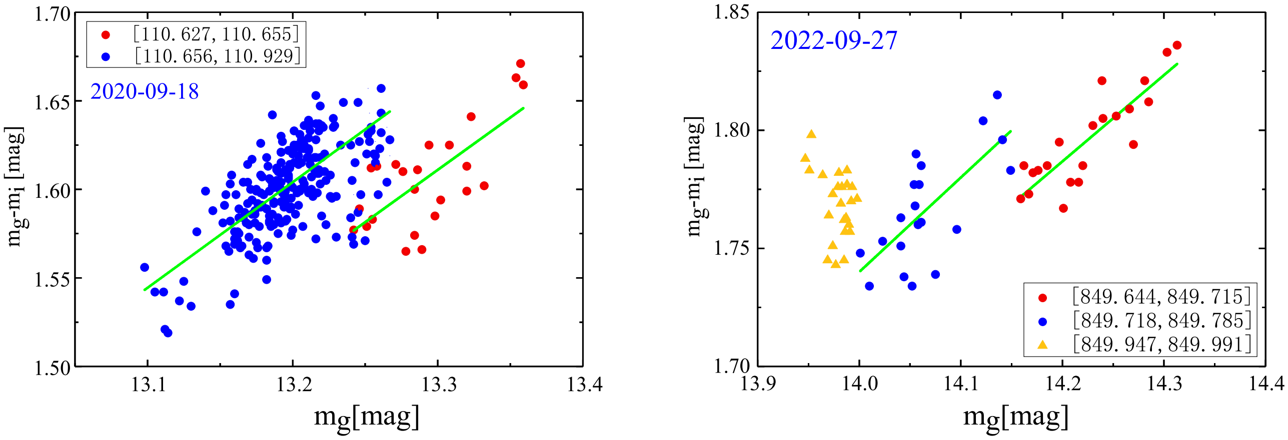

Figure 10. The correlation between the g magnitude (m_g) and color index ($m_g - m_i$), where the colored dots stand for distributions of different stages, the green lines stand for the linear fitting, and the rectangular boxes mark the time range of observations (JD +2459000).

4.3. Conclusion

In this work, we report the observations of 1ES 2200+420 within the monitored period of about 2 yr, when the source is in a very variable state and the maximum variabilities are about 2 mag. We separate the intraday lightcurves into the brightening stages and the dimming stages, and find IDV phenomena in 103 stages within 19 days. We obtained some characteristic values of IDV, including variable timescales (ΔT), variable value (Δm), and variable rate ($\frac{\Delta m}{\Delta T}$). ΔT and Δm show frequency-dependent behaviors, and with the frequency increasing, the variabilities tend to be more drastic. There are intraday periodic oscillations on 3 days, with the periods being ~150 minutes (2020 September 7), ~232 minutes (2020 September 19), and ~150 minutes (2022 September 7). This source displays strong BWB behavior on longer timescales and the time evolution of color on 2 days (2020 September 18 and 2022 September 27).

Acknowledgments

We thank the anonymous reviewer for the good suggestion. We acknowledge the science research grant from the China Manned Space Project with No. CMS-CSST-2021-A06. The work is partially supported by the National Natural Science Foundation of China (NSFC U1831119, U2031112, NSFC U2031201, NSFC 11733001) and Guangdong Major Project of Basic and Applied Basic Research (grant No. 2019B030302001). The observations were monitored by the 1.26 m NGT telescope, which is located at the Xinglong Observatory of the National Astronomical Observatories.

ORCID iDs

Y. H. Yuan https://orcid.org/0000-0001-8395-1706
J. H. Fan https://orcid.org/0000-0002-5929-0968
J. H. Yang https://orcid.org/0000-0002-4469-9672
Z. Y. Pei https://orcid.org/0000-0002-4970-3108

References

de Diego, J. A. 2010, AJ, 139, 1269
de Diego, J. A., Polednikova, J., Bongiovanni, A., et al. 2015, AJ, 150, 44
Espaillat, C., Bregman, J., Hughes, P., & Lloyd-Davies, E. 2008, ApJ, 679, 182
Fan, J. H. 2005, ChJAS, 5, 213
Fan, J. H., Xie, G. Z., Pecontal, E., Pecontal, A., & Copin, Y. 1998, ApJ, 507, 173
Fan, J. H., Yuan, Y. H., Wu, H., et al. 2019, RAA, 19, 142
Fan, J. H., et al. 2017, ApJ, 837, 45
Gaur, H., Gupta, A. C., Strigachev, A., et al. 2015, A&A, 582, A103
Gupta, A. C., Srivastava, A. K., & Wiita, P. J. 2009, ApJ, 690, 216
Heidt, J., & Wagner, S. J. 1996, A&A, 305, 42
Hervet, O., Boisson, C., & Sol, H. 2016, A&A, 592, A22
Hong, S., Xiong, D., & Bai, J. 2018, AJ, 155, 31
Itoh, R., Nalewajko, K., Fukazawa, Y., et al. 2016, ApJ, 833, 77
Jorstad, S. G., Marscher, A. P., Raiteri, C. M., et al. 2022, Natur, 609, 265
Kalita, N., Yuan, Y. H., Gu, M. F., et al. 2023, ApJ, 943, 135
Kinzel, W. M., Dickman, R. L., & Predmore, C. R. 1988, Natur, 331, 48
Lachowicz, P., Gupta, A. C., Gaur, H., & Wiita, P. J. 2009, A&A, 506, L17
Liu, X. L., Yuan, Y. H., & Huang, H. R. 2021, RAA, 21, 004
Lomb, N. R. 1976, Ap&SS, 39, 447
Marscher, A. P., Jorstad, S. G., D'Arcangelo, F. D., et al. 2008, Natur, 452, 966
Meng, N., Wu, J., Webb, J. R., Zhang, X., & Dai, Y. 2017, MNRAS, 469, 3588
Miller, J. S., French, H. B., & Hawley, S. A. 1978, ApJL, 219, L85
Mutel, R. L., & Phillips, R. B. 1987, in Superluminal Radio Sources, ed. J. A. Zensus & T. J. Pearson (Cambridge: Cambridge Univ. Press), 60
Nilsson, K., Lindfors, E., Takalo, L. O., et al. 2018, A&A, 620, 185
Papadakis, I. E., Boumis, P., Samaritakis, V., & Papamastorakis, J. 2003, A&A, 397, 565
Raiteri, C. M., Villata, M., D'Ammando, F., et al. 2013, MNRAS, 436, 1530
Sahakyan, N., & Giommi, P. 2022, MNRAS, 513, 4645
Sandrinelli, A., et al. 2017, A&A, 600, A132
Scargle, J. D. 1982, ApJ, 263, 835
Schulz, M., & Mudelsee, M. 2002, CG, 28, 421
Sitko, M. L., Schmidt, G. D., & Stein, W. A. 1985, ApJS, 59, 323
Smith, P. S., Balonek, T. J., Heckert, P. A., Elston, R., & Schmidt, G. D. 1985, AJ, 90, 1184
Stickel, M., Fried, J. W., Kuehr, H., Padovani, P., & Urry, C. M. 1991, ApJ, 374, 431
Ulrich, M. H., Maraschi, L., & Urry, C. M. 1997, ARA&A, 35, 445
Urry, C. M., & Padovani, P. 1995, PASP, 107, 803
Urry, C. M., et al. 1993, ApJ, 411, 614
Valtaoja, E., Lehto, H., Teerikorpi, P., et al. 1985, Natur, 314, 148
Vermeulen, R. C., & Cohen, M. H. 1994, ApJ, 430, 467
Villata, M., Raiteri, C. M., Aller, H. D., et al. 2004, A&A, 424, 497
Villata, M., Raiteri, C. M., Larionov, V. M., et al. 2009, A&A, 501, 455
Visvanathan, N., & Elliot, J. L. 1973, ApJ, 179, 721
Weaver, Z. R., Williamson, K. E., Jorstad, S. G., et al. 2020, ApJ, 900, 137
Xiong, D., Bai, J., Zhang, H., et al. 2017, ApJS, 229, 21
Yuan, Y. H., & Fan, J. H. 2021, PASP, 133, 074101
Yuan, Y. H., Wang, G. G., Xiao, H. B., et al. 2022, ApJS, 262, 43